ROYAL SOCIETY
OF CHEMISTRY

PAPER

A one-dimensional perovskite with ferroelectric and switchable nonlinear optical properties: [azetidinium]CdCl₃†

Magdalena Rok, [ID] *[a] Bartosz Zarychta, [ID] [b] Joanna Trojan-Piegza, [ID] [a]
Andrzej Bil, [ID] [a] Anna Piecha-Bisiorek, [ID] [a] Jan K. Zaręba, [ID] [c]
Wojciech Medycki [ID] [d] and Ryszard Jakubas [ID] [a]

Organic–inorganic perovskite hybrids (OIPHs) have been a topical area of interest in recent years. This stems from their key features such as facile and inexpensive solution based synthesis, high mechanical flexibility, structural tuneability, and chemical diversity, to name a few. Additionally, the frequently observed emergence of ferroelectric or piezoelectric properties along with optical properties renders them promising for photovoltaic energy conversion or mechanical energy harvesting applications. Herein, we report the synthesis of a novel ABX₃-type ferroelectric crystal **AZECdCl₃** of formula [C₃H₈N]CdCl₃, forming an infinite one-dimensional [{CdCl₃}⁻]ₙ chain along the *c* direction, with azetidinium (AZE) cations C₃H₈N⁺ fitted in-between the inorganic chains. Calorimetric (DSC) measurements revealed that the crystal undergoes a complex sequence of phase transitions, at 495 K (discontinuous **I → II**), 202 K (continuous **II → III**) and 167K (discontinuous **III → IV**). **AZECdCl₃** is characterised by a strongly enhanced electric permittivity around the paraelectric–ferroelectric transition at 202 K, exhibiting excellent ferroelectric hysteresis loops with a spontaneous polarization (P_s) of 4 μC cm⁻² (168 K) and with a relatively small coercive electric field (E_c) of 1.02 kV cm⁻¹. The crystal exhibits also ferroelastic properties over all low temperature phases. The experimental value of P_s agrees with theoretical predictions based on density functional theory-based calculations. The temperature-resolved second-harmonic generation (SHG) measurements attest to the polar order of this phase. First-order phase transition **IV ↔ III** was demonstrated to feature robust, high contrast SHG-off–SHG-on switching functionality. The broadband luminescence reveals thermal quenching when going from cryogenic temperatures to room temperature. The emission was assigned to the synergistic emissions of excitons due to the structural deformation of the lattice.

1. Introduction

Ferroelectrics based on organic–inorganic hybrids, although have been around for some time, still attract considerable attention as a potential alternative to conventional perovskite

[a] *Faculty of Chemistry, University of Wroclaw, 14 F. Joliot – Curie, 50-383 Wroclaw, Poland. E-mail: magdalena.rok@chem.uni.wroc.pl*
[b] *Faculty of Chemistry, University of Opole, Oleska 48, 45-052 Opole, Poland*
[c] *Advanced Materials Engineering and Modelling Group, Faculty of Chemistry, Wrocław University of Science and Technology, Wybrzeże Wyspiańskiego 27, 50-370 Wrocław, Poland*
[d] *Institute of Molecular Physics, Polish Academy of Sciences, Smoluchowskiego 17, 60-179 Poznań, Poland*

oxide materials. Their intrinsic merits are the diversity of tunable structures, mechanical flexibility and a wide range of synthetic conditions that can be employed for synthesis. Some ferroelectric hybrids have recently been employed in applications such as detectors, FeRAMs, photovoltaics, and mechanical energy harvesters, thus tying up with important facets of modern economy.[1–8] In this regard, much attention has been paid to hybrids with perovskite-type compositions of the general formula ABX₃, where A stands for an organic cation, B for a transition metal atom, and the bridging ligand X is the halogen anion.

Among ABX₃ compounds, there has been a growing body of reports on the electrical properties of crystals containing Cd(II).[9–13] Take, for example, ferroelectric hybrid [(CH₃)₄P]CdCl₃,[14] which has a relatively high Curie temperature (T_c = 348 K) and remnant polarization (P_r = 0.43 μC cm⁻²) compared to its isostructural analogue [(CH₃)₄N]CdBr₃.[15] It has also been proven that doping of Sb(III) in

3036 | *J. Mater. Chem. C*, 2022, **10**, 3036–3047

This journal is © The Royal Society of Chemistry 2022

crystals generated photoluminescence in the tested hybrid materials. The incorporation of the 3-pyrrolinium[16] cation into the A position of the ACdCl$_3$ system increases the polarization value to 5.1 μC cm^{-2}, compared to the pyrrolidinium[17] cation for which P_s was 3.6 μC cm^{-2}. Interestingly, the use of a chiral cation in the (R)- and (S)-3-F-(pyrrolidinium)CdCl$_3$ system guarantees a stable ferroelectric with a high transition temperature (T_c), which is essential for the practical utility of ferroelectric devices.[18]

Additionally, ferroelectric materials based on organic–inorganic hybrids from the halogen–metal family have recently attracted much attention due to the possibility of using them in electricity (nano)generators.[19–22] Commonly used inorganic piezoelectric materials based on zinc oxides, barium titanate, lead zirconate titanate and others[23–26] are not flexible enough for this purpose. OIPHs appear to be perfect alternatives to inorganic counterparts, given their mechanical flexibility and ease of obtaining thin layers. The first one-dimensional hybrid, for which mechanical energy harvesting was achieved, was that with the general formula [Me$_3$NCH$_2$CH$_2$OH]CdCl$_3$,[19] generating a very high polarization of 17.1 μC cm^{-2}. High values of spontaneous polarization are also observed for materials of the A$_2$BX$_4$ stoichiometry. In the case of [BnNMe$_2$R]$_2$CdBr$_4$ (Bn = benzyl; 1: R = Me; 2: R = n-Pr)[20] crystals the P_s equals 18.59 and 14.24 μC cm^{-2}, respectively. Due to the attractive electrical properties, such as a high polarization value and electric permittivity, these materials can be used to create polydimethylsiloxane (PDMS) polymer composite samples. These devices were tested for their mechanical energy harvesting functionality, and the results obtained encourage the design and development of new types of ferroelectric hybrids and their use in self-powered electronics.

In addition to the apparent benefits of ferroelectricity, switching of second harmonic generation (SHG) between states of different activities due to the temperature change has become an exciting new branch of materials science. Recently, organic–inorganic hybrids based on halide derivatives of Cd(II) have been employed in the field of nonlinear optical switching. Specifically, for [pyrrolidinium]CdCl$_3$[17] SHG-off–SHG-on–SHG-off has been demonstrated for the first time owing to a rarely observed sequence of phases in which a non-centrosymmetric phase is "in-between" the two centrosymmetric phases. Understanding the mechanism of phase transition (PT) that results in SHG quenching during the cooling process may be helpful in designing new switchable NLO materials with unusual SHG-off–SHG-on functionality.

Encouraged by the structural tunability of perovskite compounds and their electrical and NLO properties, we synthesized a new organic–inorganic hybrid material crystallizing with ABX$_3$ stoichiometry in which A and B sites are occupied by azetidinium, and cadmium(II) ions, respectively. The compound undergoes three-stage phase transitions, in which only one phase (III) is polar and exhibits ferroelectric properties. The molecular dynamics of the polar cation was investigated using ^{1}H NMR measurements in the solid-state. The crystal under investigation was explored using dielectric spectroscopy, pyroelectric tests, and temperature-resolved second harmonic

generation (TR-SHG) measurements, and was tested for polarization switching properties. For instance, metal ions with a d^{10} configuration, Zn^{2+}, Cd^{2+} and Hg^{2+}, can act as luminescence centres to achieve a broadband emission. In this context, the reported **AZECdCl$_3$** is expected to serve as a right candidate for luminescence predominantly ascribed to the self-trapping exciton[27] associated with structural deformations.[28] Since the structure and its distortions play an essential role in defect localization and exciton creation, they further help in determining the optical properties of the **AZECdCl$_3$** crystal. Thus, the temperature-dependent luminescence of **AZECdCl$_3$** was studied and assigned to the combination of free-excitonic emission and self-trapped excitonic emission.

2. Results and discussion

2.1. X-ray crystal structure analysis

The structure of **AZECdCl$_3$** was determined at 220.0(1) (phase **II**, $Cmcm$), 185.0(1) (phase **III**, $Cmc2_1$) and 100.0(1) K (phase **IV**, $Pbnm$). The structure at 100.0(1) K was originally solved in the $Pnma$ space group. However, the final model was refined in a non-standard setting to match cell parameters from high-temperature phases, i.e., $Pbnm$. Moreover, the asymmetric parts of the unit cells and the labelling of atoms at all temperatures have been chosen to show the structural relationship between the positions of the corresponding atoms in phases (Fig. 1). In all phases, the anionic substructure is composed of distorted [CdCl$_6$]$^{4-}$ octahedra that share all six corners with two other neighbours, forming infinite one-dimensional [{CdCl$_3$}$^-$]$_n$ chains arranged in the c direction. The azetidinium cations C$_3$H$_8$N$^+$ are located between the inorganic chains. The crystal data and the structure determination details are listed in Table S1 (ESI†). The bond lengths, valence and torsion angles, and hydrogen bond geometries are presented in Tables S2 and S3 (ESI†).

At 220 K, in the independent part of the unit cell, there is one central cadmium(II) atom surrounded by two crystallographically independent chlorine ligands and one disordered quarter-molecule of the azetidinium cation. Because of the dynamical disorder, the N–C, C–C bond lengths and N(C)–C(N)–C angles were not determined with high precision. The disorder model suggests that the cation dynamics could be described as wobbling motion around a positively charged nitrogen atom and the opposite C3 atom in a perpendicular direction (Fig. 2). The cation is held by relatively weak intermolecular interactions of N–H···Cl and C–H···Cl types with a shortest N(C)···Cl distance of 3.374 (10) Å and 3.57 (2) Å for N and C, respectively.

At 185 K, the structure of **AZECdCl$_3$** belongs to the polar space group of $Cmc2_1$. The transition triggers significant symmetry transformation i.e., the crystallographic symmetry elements vary from (E, C_2, C_2', C_2'', i, σ_h, σ_v, and σ_v') at 220 K to (E, C_2, σ_v, and σ_v') at 185 K. The lowering of the temperature leads to partial freezing of the cation reorientational motion (Fig. 2b). The cations adopt one of the disordered positions
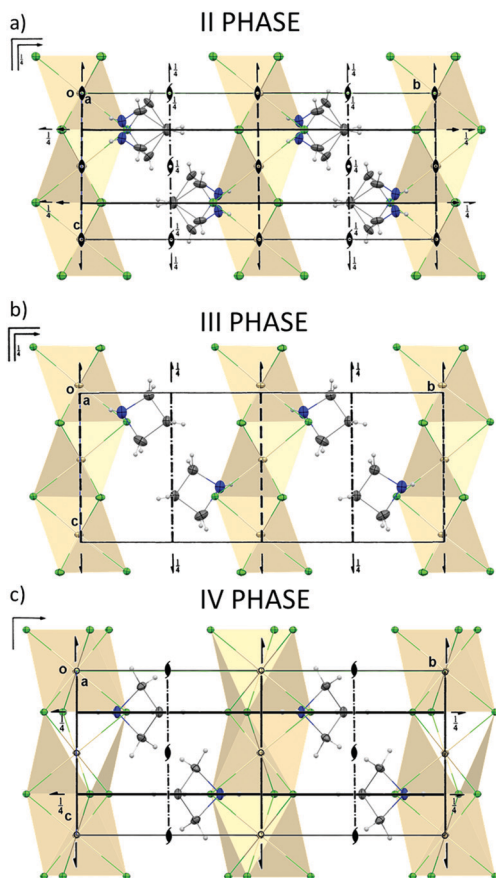
This journal is © The Royal Society of Chemistry 2022

J. Mater. Chem. C, 2022, **10**, 3036–3047 | 3037

Fig. 1 Unit cell packing of **AZECdCl₃** in phase **II** (a), **III** (b) and **IV** (c) in the [100] direction along with a projection of cell's symmetry elements. Thermal ellipsoids are drawn at 25% probability level.
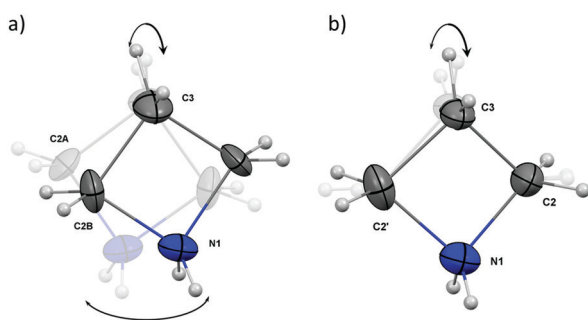

Fig. 2 Disorder model of **AZECdCl₃** at 220 K (a) (phase **II**) and 185 K (b) (phase **III**). Only symmetrically independent part is labelled; thermal ellipsoids are drawn at 25% probability level.

from the structure at 220 K. This change rebuilds the symmetry of the unit cell by deletion of the σ'_v mirror plane. Moreover, the new position of the cation influences the mean direction of the dipole moment, which points now along the [001] direction. Upon temperature lowering, there is no significant change in the amount and strength of the intermolecular interactions, and the difference in D···A distances does not exceed 2σ in value.

In the low-temperature phase (**IV**), the structure of **AZECdCl₃** is still orthorhombic (space group *Pbnm*). Here the number of the crystallographic symmetry elements is increased back as the symmetry changes from (E, C_2, σ_v, and σ'_v) at 185 K to (E, C_2, C'_2, C''_2, i, σ_h, σ_v, and σ'_v) at 100 K. This difference is attributed to the changes in both: organic cation dynamics and a deep structural transformation of the inorganic substructure. In phase **IV**, the molecule motions are firmly frozen. The molecule twists around the a direction and adopts a C_{2v} symmetry at the special position of the unit cell's, generating the σ'_v mirror plane (Fig. 1c). As presented in Fig. 3, during **III** → **IV** PT the inorganic and organic substructures are twisted by *ca.* 12.6° and 37.6°, respectively, around the c direction. By contrast, during **II** → **III** PT, no such rotation is observed.

In phase **IV**, the ordered cation participates in stronger N–H···Cl hydrogen bonds as the distance between donor and acceptor decreases from 3.38(1) Å to 3.16(1) and 3.28(1) Å. This corresponds well with the twist of the organic substructure to the direction of the inorganic framework.

In all phases, the octahedral coordination of Cd(ɪɪ) is distorted, and the distortion changes on lowering the temperature. A measure of the Cd(ɪɪ) deformation can be estimated by eqn (1) by calculating the distortion parameter Δ if one takes bond lengths into account.

$$\Delta = \frac{1}{6} \sum_{i+1}^{N} \left(\frac{R_i - \bar{R}}{\bar{R}} \right)^2 \times 10^4 \qquad (1)$$

where $\bar{R}$ is the average Cd–Cl bond length within the octahedron and R_i is the individual Cd–Cl bond length. For the valence angles, the distortion of the octahedral coordination can be easily estimated with the use of corrected sample standard deviation, in which the expected value amounts to 90° for *cis* angles (variance of the octahedral angles) (eqn (2)).[29]

$$\sigma_{cis}^2 = \sqrt{\frac{1}{N-1} \sum_{i=1}^{N} (x_i - 90°)^2} \qquad (2)$$

The Δ parameter in phases **II** (220 K) and **III** (185 K) differs only by 0.1 (0.89 *vs.* 0.99, respectively). However, in the low temperature phase (**IV**), the octahedron deformation increases
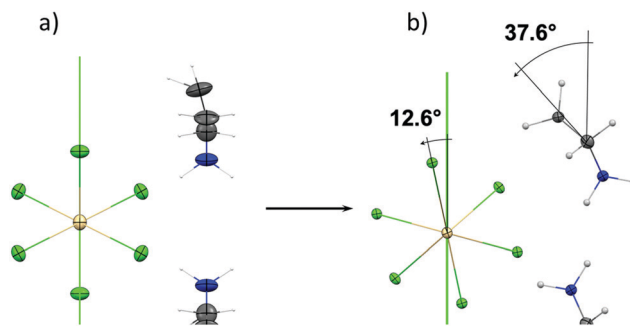

Fig. 3 Projection (along the c direction) of the structural changes in inorganic and organic substructures between phases **III** (a) and **IV** (b) in **AZECdCl₃**. Thermal ellipsoids are drawn at 25% probability level.

3038 | *J. Mater. Chem. C*, 2022, **10**, 3036–3047

This journal is © The Royal Society of Chemistry 2022

radically as the parameter increases by *ca.* 80% (1.79). When *cis* angles are taken into account, the main deforming factor is the type of the inorganic structure (face connected octahedra). However, the PTs also influence this relatively rigid arrangement. The σ_{cis} parameter is the largest for the polar structure at 185 K (**III**) as it amounts to 6.65°, making it the most distorted octahedron across all phases. Nevertheless, the parameter at 220 K differs only slightly (6.55°), while at phase **IV**, the parameter changes by *ca.* 12% ($\sigma_{cis} = 5.83°$). This effect is also noticeable for the *c* parameter and Cd–Cd distances between adjacent octahedra (Table S2 in ESI†). The *cis* angle deformation increases as the Cd–Cd distance increases.

The analysis of the contact surface, upon the azetidinium cation removal, shows a decrease of the volume of the inorganic framework cages with the temperature lowering. In the **II** → **III** PT, the surface volume for $(C_3H_8N)CdCl_3$ decreases only slightly by 0.2% for the unit cell volume. Nevertheless, the **III** → **IV** PT causes a dramatic structural change in the value of the contact surface. The volume decreases here by 13.5% from 336.95 Å^3 to 288.28 Å^3 justifying large-scale changes in the inorganic substructure.

2.2. Thermal analysis

The DSC traces for **AZECdCl₃** are presented in Fig. 4. The thermal analysis was performed as follows. First, the sample was cooled from room temperature (RT) to 140 K, and then heated to 500 K. The last cycle was performed on cooling from 500 K to RT. DSC measurements revealed that below RT, there are two reversible thermal anomalies assigned to structural PTs, *i.e.* at 202/202 K (cooling/heating) and 164/167 K. The evident thermal hysteresis and sharp heat anomaly both indicate the first-order feature of the (**III** → **IV**) PT. By contrast, the higher temperature weak anomaly is characteristic for the second-order PT, marked as (**II** → **III**). Based on the Boltzmann equation $\Delta S = R \ln N$, the ratio of the respective numbers of microstates N below and above PT can be estimated. In the case of the **IV** → **III** PT, the parameter N is equal to *ca.* 4.7 suggests an order–disorder nature of this transition. In turn, the heating of **AZECdCl₃** above RT disclosed a weak thermal anomaly a few

degrees below the decomposition point of the sample, which means that the crystal is stable up to the temperature of 500 K (Fig. S1 in the ESI†). The shape of this hardly reversible thermal anomaly suggests the discontinuous nature of PT (**II** → **I**, at 495 K), whereas the estimated value of $N \approx 1.2$ suggests a ''displacive'' mechanism.

2.3. Temperature-resolved second harmonic generation (TR-SHG) measurements

Next, we have turned to temperature-resolved second harmonic generation (TR-SHG) measurements to provide spectroscopic evidence for (non)centrosymmetry of observed crystal phases of **AZECdCl₃**. TR-SHG measurements were performed in the 145–220 K range (both heating and cooling runs) by irradiation with 800 nm femtosecond laser pulses. Experimental SHG spectra for heating and cooling runs are provided in Fig. S2 and S3 (ESI†), respectively. Fig. 5a shows that the SHG signal is present for phase **III** only. More specifically, one sees that upon heating from 140 K upwards, the SHG signal starts increasing at *ca.* 155 K to reach the maximum at 165 K; after that point the SHG response slowly decreases in a nearly linear fashion to disappear at *ca.* 202 K, thus completing the plot of 'sawtooth' type. The subsequent cooling run shows that the SHG response
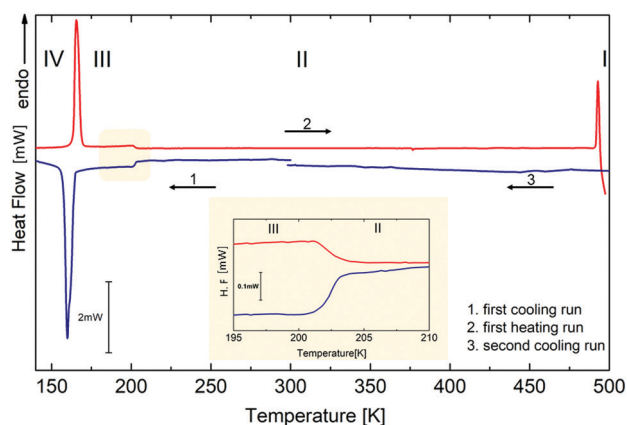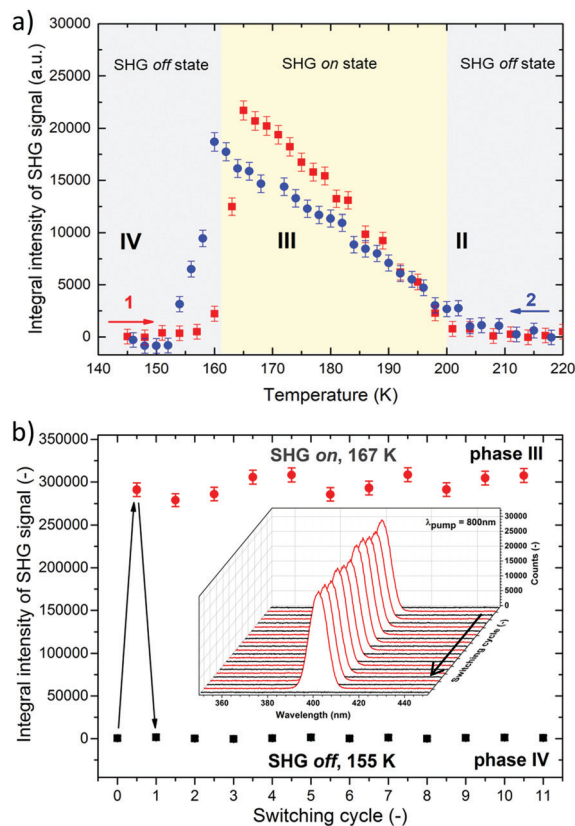

Fig. 5 (a) Integral intensities of the SHG signal (400 nm) for **AZECdCl₃** plotted as a function of temperature. (b) Plot of integral intensities of SHG signals obtained during the switching experiment between 155 K (black squares) and 167 K (red circles). The inset presents the corresponding experimental spectra of the obtained SHG responses.

Fig. 4 DSC traces for **AZECdCl₃** between 145 and 500 K (scanning rate 5 K min⁻¹ and m = 8.5080 mg).

This journal is © The Royal Society of Chemistry 2022

J. Mater. Chem. C, 2022, **10**, 3036–3047 | **3039**

gradually increases when the temperature decreases from 202 K down to 160 K. Below that temperature point, the SHG signal is absent. From these results it is apparent that transition $III \rightarrow IV$ is characterized by ~ 5 K thermal hysteresis, confirming the first order character of this PT. On the other hand, both the lack of thermal hysteresis as well as slow build up and decay of the SHG response in 160–202 K range attest to the continuous nature of $II \rightarrow III$ structural transformation.

We have also assessed the relative SHG efficiency of **AZECdCl$_3$** by means of the Kurtz–Perry powder test on size-graded samples. Since in the case of **AZECdCl$_3$**, the strength of second-order NLO activity varies across a broad temperature range, relative SHG efficiency was determined at a temperature at which the maximal nonlinear response was registered (165 K). Accordingly, one sees that upon 800 nm irradiation **AZECdCl$_3$** generates second harmonics of radiation equal to 0.12 of that of KDP with the same particle size. The collected results thus show that phase the transition sequence of SHG-off $\leftrightarrow$ SHG-on $\leftrightarrow$ SHG-off states is present here, which offers prospects for quadratic NLO switching between active and inactive NLO states. It is worth noting that the same pattern of noncentro and centrosymmetric phases was previously observed for the [pyrrolidinium]CdCl$_3$[17] material, for which switching between one NLO-active state and two NLO-inactive states was demonstrated (switching of the off–on–off type).

In the case of **AZECdCl$_3$** we have also explored SHG switching capability, but the selection of suitable phases for this purpose deserves a comment. Namely, the phase transition between phase **II** and phase **III** is continuous, and as Fig. 5a shows, the transition from a completely SHG-on to SHG-off state requires the temperature change of at least 45 K. Such a broad temperature window makes the practical utility of the $II \leftrightarrow III$ transition for switching purposes rather questionable, since switching requires not only a sharp change in the SHG response, but should be also performed using the smallest possible temperature step. Accordingly, we have explored $III \leftrightarrow IV$ phase transition only in terms of SHG signal switching functionality.

In the SHG switching experiment the temperature was varied in a periodic manner between the two temperature points: 155 K and 167 K, which correspond to completely converted SHG-on (**IV**) and SHG-off (**III**) states, respectively. The results are shown in Fig. 5b, which displays integral intensities of SHG collected during the switching experiment while corresponding the experimental spectra of the SHG signal are displayed in the inset. One sees that the registered SHG signals for phase **IV** do not attenuate for at least 11 switching cycles, but rather oscillate within a narrow range. On the other hand, there is no residual SHG signal for phase **III**, attesting to its complete conversion to centric setting. Accordingly, it is clear that **AZECdCl$_3$** displays reversible SHG-off–SHG-on switching functionality in a low temperature range. It can be also seen that this kind of SHG switch features very high contrast as its operates against essentially zero background.

We also note that the SHG-off–SHG-on switching scheme presented here for **AZECdCl$_3$** stands out in the context of extant binary NLO switches. Indeed, the literature search shows that the most common is the variant in which the phase below T_c is SHG-active and that above T_c is SHG-inactive, that is, the SHG-on–SHG-off switching scheme is the most widespread across solid-state NLO switches.[30–35]

2.4. Screening ferroelastic PTs

The thermal evolution of the ferroelastic domain structure, observed under a polarizing microscope, is illustrated in Fig. 6. In phase **II**, the monodomain samples of **AZECdCl$_3$** is in the form of pristine single crystals, without any external strain applied (Fig. 6a). No visible changes were observed on the crystal surface upon cooling from phase **II** to **III**. Subsequent lowering of the temperature causes the transition from phase **III** to **IV**, leading to substantial structural changes that affect the crystals' image in polarized light. As shown in Fig. 6b, the strong distortion of the crystal lattice during PT leads to the appearance of ferroelastic domains parallel to the c-axis. PT $I \rightarrow II$ leads to the paraelastic phase. Most likely, we deal with the orthorhombic $\leftrightarrow$ tetragonal transitions.

Strong distortion of the crystal lattice during each PT usually leads to cracking of the single-crystal sample. After heating to phase **III**, we still observe domains that persist in phase **II** (Fig. 6c). As shown in Fig. 6d, re-cooling to phase **IV** sharpens the ferroelastic domains and causes further crystal destruction. The appearance of ferroelastic domains may indicate that high-temperature phase **I** is the prototype/paraelastic one, and the transition from phase **II** to **I** can be classified as ferroelastic–paraelastic. The consequence of PT from the ferroelastic to the paraelastic phase is a change in the crystallographic system, and additionally, all the elements of the ferroelastic phase symmetry should be included in the paraelectric set. Since the image lacks domains that would intersect at an angle of 60 or 120°, this may suggest that the prototype phase cannot be trigonal or hexagonal and tetragonal is most likely.

2.5. Electric properties

The dielectric response, presented in Fig. 7, was measured for a single-crystal sample along the polar direction (c-axis), while Fig. S4 (ESI†) shows the temperature dependence of the complex dielectric permittivity ε^* measured perpendicular to a- and b-axes. By comparing the results obtained for these three directions, the most noticeable changes in the vicinity of PT are seen along the polar c-axis, which also indicates the strong dielectric anisotropy. The ferroelectric nature of the transition
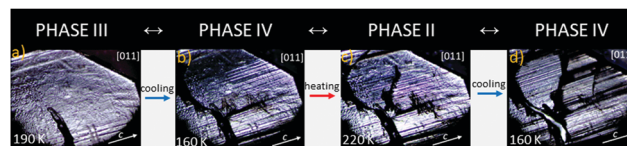

Fig. 6 The evolution of the domain structure for **AZECdCl$_3$** with the direction perpendicular to the largest face [011] of the relatively thin as-grown plate. (a and b) The first cycle on cooling from phase **III** to **IV**. (b and c) Next heating from phase **IV** for phase **II**. (c and d) The last cooling from phase **II** to **IV**.
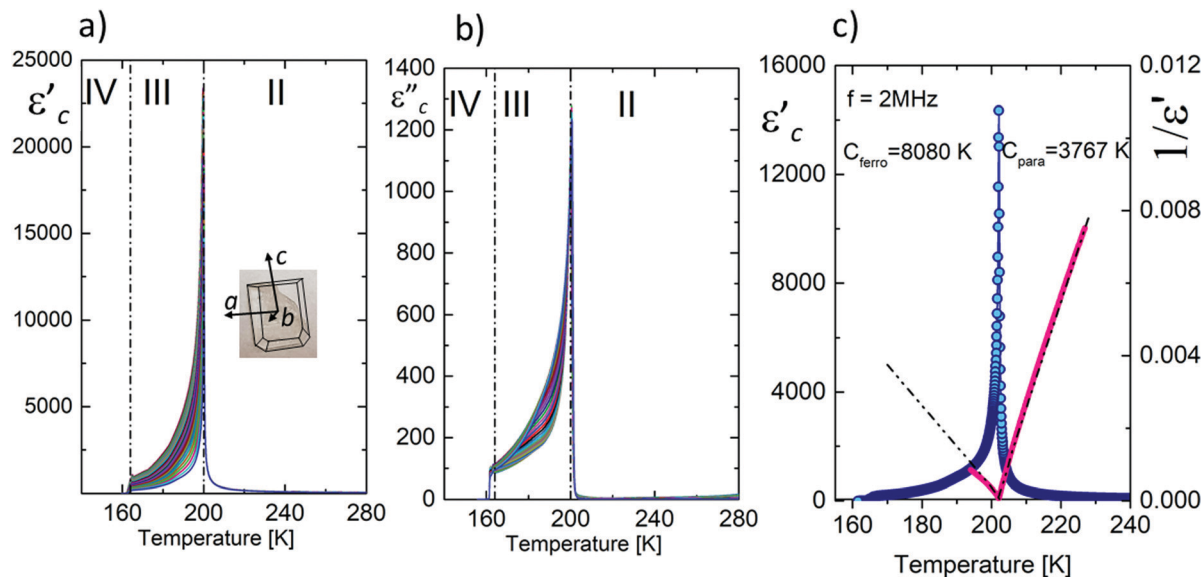
3040 | J. Mater. Chem. C, 2022, **10**, 3036–3047

This journal is © The Royal Society of Chemistry 2022

Fig. 7 The temperature dependence of the dielectric permittivity, (a) ε' and (b) ε'' obtained on cooling run for single crystals along the c-axis ($S = 4$ mm^2 and $d = 1.1$ mm). The range of frequency was from 500 Hz to 2 MHz. (c) The dielectric Curie–Weiss law around the ferroelectric transition for a frequency of 2 MHz.

is evident from the critical anomaly of the electric permittivity (ε'), being close to the Curie temperature ($T_C = 202$ K). The temperature-dependent real part (ε') of permittivity at each frequency shows a distinct λ-shape peak through the T_c, with large values for ε' of 13 000–25 000 (for the frequency range of 135 Hz–2 MHz), indicating that phase **III** possesses a ferroelectric nature. Additionally, in the vicinity of T_c, ε' follows the Curie–Weiss law, i.e. $\varepsilon' = C_{para}/(T - \theta)$, where ($T > T_c$) or $C_{ferro}/(\theta' - T)$ where ($T < T_c$). The C_{para} and C_{ferro} are the Curie–Weiss constants of **II** and **III** phases, and their values obtained from the fitting are 3767 and 8080 K for paraelectric and ferroelectric phases, respectively. The fitting gives a C_{para}/C_{ferro} ratio (2.14), which is close to the theoretical value of 2 expected for the second-order ferroelectric transition. The Curie–Weiss temperatures ($\theta = 202.3$ K, $\theta' = 201.9$ K) are very close to $T_c = 202$ K. In the case of the dielectric results presented in a logarithmic scale (y-axis), relaxation processes of disparate nature are much more apparent for paraelectric and ferroelectric phases (Fig. S5, ESI†). It is clearly seen (Fig. 7a and b) that the ferroelectric transition **II** → **III** is immediately followed by a relaxation process, which corresponds to the relaxation of the domain/domain boundary formed/reformed as a result of that particular ferroelectric transition. However, it should be added that the dynamic properties within ferroelectric phases are usually complex. If dielectric relaxation appears below T_c (Curie temperature), it may have a different mechanism. Generally, at low temperatures, we have so-called two origins: (i) the "extrinsic" contribution, which is mainly attributed to domain wall motions and (ii) "intrinsic" contributions, which originate from the dielectric (maybe dynamics of dipolar molecules) and piezoelectric responses of single domain samples. Taking into account the dielectric response of **AZECdCl$_3$** in the close vicinity of T_c we deal with the "displacive" mechanism of ferroelectric

transitions. In the case of the order–disorder mechanism in ferroelectrics in the vicinity of T_c we should observe a critical slowing down of the macroscopic relaxation time,[36] which do not appear up to 2 MHz. However, considering the order–disorder mechanism proposed based on crystallographic results, one can expect the ferroelectric relaxation in the gigahertz frequency region (above 1 GHz).

Nevertheless, the displacive mechanism is dominant, whereas the possible order–disorder one plays a negligible role. The question of dielectric relaxation and its possible sources are presented in Fig. S6 (ESI†), showing the frequency dependence of the electric permittivity for selected temperatures obtained in both paraelectric (**II**) and ferroelectric (**III**) phases. The determined activation energy is 27.22 kJ mol^{-1} and is assigned to the domain-wall motion. On the other hand, traces of the relaxation process barely visible near T_c in the paraelectric phase may be related to the dynamics of dipolar molecules with a dispersion maximum in the GHz region. In order to check the ferroelectricity of **AZECdCl$_3$**, the hysteresis loop (P–E) was measured on a single crystal sample along the polar c-axis. In Fig. 8a, we can observe well-shaped rectangular P–E hysteresis loops for selected temperatures at a frequency of 1 Hz with a relatively large saturation polarization (P_s) of 4 μC cm^{-2} (168 K), and with a relatively small coercive electric field (E_c) of 1.02 kV cm^{-1}. Similar results were obtained for the closely related compound, [pyrrolidinium]CdCl$_3$,[17] where the coercive field was also small (1.5 kV cm^{-1}), and P_s was equal to 3.6 μC cm^{-2}. Fig. 8b depicts a typical IC–E (instantaneous current density–electric field) curve with two opposite peaks due to charge displacement, corresponding to two stable states with opposite polarity. Fig. 8b diagram also shows the decrease of the coercive field when the temperature increases. The frequency dependency of the P–E loop is illustrated in
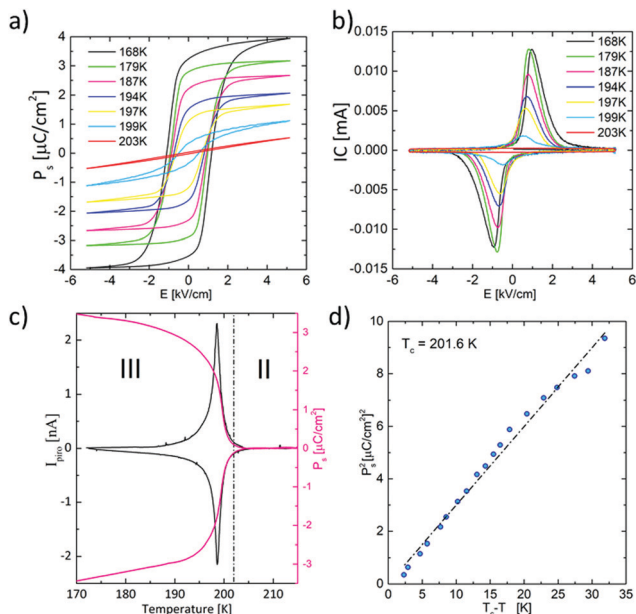
This journal is © The Royal Society of Chemistry 2022

J. Mater. Chem. C, 2022, **10**, 3036–3047 | **3041**

Fig. 8 (a) Polarization−electric field (P−E) hysteresis loops measured for the chosen temperatures (max. electric field of 5.21 kV cm^{-1}, f = 1Hz). (b) IC−E (instantaneous current (mA) density−electric field) curve with two opposite peaks (max. field 5.21 kV cm^{-1}, f = 1Hz). (c) Temperature dependence of I_{pyro} (black line) measured for a sample after the application of the DC electric field ($\pm$1.32 kV cm^{-1}) in phase **II** and then cooling the sample to phase **III**. The measurements of I_{pyro} were carried out during heating (**III** → **II**). Polarization $P_s(T)$ (pink line) determined by the integration of the pyroelectric current. (d) P_s^2 versus (T_c − T), fitted T_c equals 201.6 K.

Fig. S7a (ESI†) for the range between 1 and 2000 Hz. According to these data, some slight decrease in both P_r and E_c is observed when the frequency increases. Similar results were obtained for $[(CH_3)_4P]CdCl_3$.[14] The evolution of the loop saturation for 1 Hz is shown in Fig. S7b (ESI†).

As shown in Fig. 8c, the temperature-dependent polarization was calculated by integrating the pyroelectric current. As can be seen, a sharp peak of pyroelectric current is formed near T_c, which inverts as the direction of the applied field changes, with an intensity of 1.32 kV cm^{-1}. The obtained polarization of about 3.5 μC cm^{-2} (for 170 K) matched well the value measured from the P–E loop. The linear dependence of P^2 vs. (T_c − T) presented in Fig. 8d also indicates the continuous nature of the PT with the estimated temperature T_c = 201.6 K.

2.6. Spontaneous polarization – theoretical calculations

Quantum mechanical calculations offer a supplementary approach to studying the electronic structure of crystals. In particular, for a well-defined (ordered) phase, the components of spontaneous polarisation can be calculated. For non-centrosymmetric phase **III** of **AZECdCl₃**, such calculations can be performed only if the original disordered phase can be properly modelled using ordered structures. To this end, we prepared two sets of coordinates (A and B, see in Fig. S8, ESI† for details) by setting the position of azetidinium cations, whose reorientational motions between two symmetrically equivalent positions are the origin of the disorder of phase **III**.

Within this model, which bases on the crystal structure measured at 185 K, the spontaneous polarization of phase **III** can be obtained by averaging the polarizations calculated for the ordered structure represented by A and B. Consequently, the only non-vanishing component of the spontaneous polarization is the one directed along 'c'.

The calculated length of the spontaneous polarisation vector falls in a narrow range of 3.0–3.1 μC cm^{-2} depending on the density functional applied for the calculations, which agrees with the experimental data. Due to a non-periodic character of the position operator, the calculated value of spontaneous polarization is inherently accompanied by a so-called polarization indetermination quantum,[37,38] (see further details in Table S5 and S6 in the ESI†). The agreement between the experimental and the theoretical spontaneous polarization indicates that the basic value reported here is physically meaningful. Interestingly, the length of the 'a' component of the spontaneous polarization calculated for the ordered model derived from phase **III** is small, i.e. below 0.2 μC cm^{-2}.

2.7. ^{1}H NMR studies

Temperature dependence of ^{1}H NMR spin–lattice relaxation time T_1 is shown in Fig. 9. Going from the lowest temperatures, the relaxation time linearly shortens from about 19.5 s at 85 K to about 6.5 s at 160 K. The value of activation energy calculated from the slope of log plot has been estimated to be 1.5 kJ mol^{-1}. Such a slight slope of the temperature dependence of the longitudinal relaxation T_1 may denote the domination of the quadrupole interaction with chlorine nuclei[39,40] in the lowest temperatures reached in the present study. Above the sudden drop of relaxation time T_1 to about 1 s at the PT, the well symmetric minimum is visible at around 218 K with a T_1 minimum of 74 ms. However, it should be noted that there is a slight discontinuity around 202 K despite the general impression that we have one symmetrical minimum of longitudinal relaxation times. In the temperature range covering phase **III**, it was only possible to determine the activation energy from the slope, which is equal to 22.1 kJ mol^{-1} (E_{a2}). Considering the
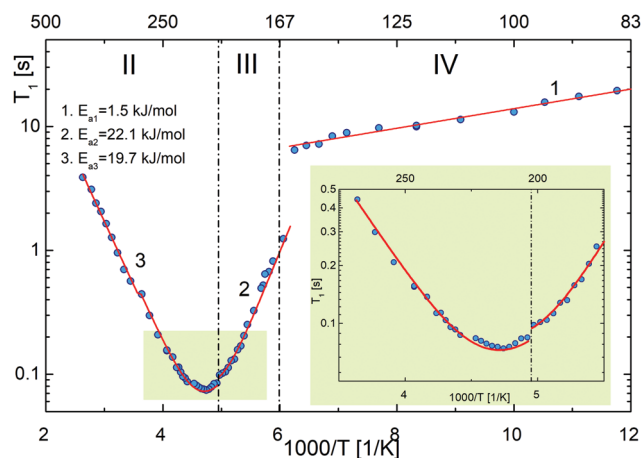

Fig. 9 Temperature dependence of the ^{1}H NMR spin–lattice relaxation time T_1 of **AZECdCl₃**.

structural results for phase **III**, this activation energy is assigned to the ring-puckering motion of the pyrrolidinium cations. In turn, the remaining points above the PT at 202 K and an observed single minimum of proton relaxation can be described by the BPP formula:[41]

$$\frac{1}{T_1} = C\left(\frac{\tau_c}{1 + \omega_0^2\tau_c^2} + \frac{4\tau_c}{1 + 4\omega_0^2\tau_c^2}\right) \quad (3)$$

Eqn (3) represents the Larmor resonance angular frequency (ω_0), C – relaxation constant, and the correlation time (τ). The Arrhenius law describes the temperature dependence of correlation time: $\tau_c = \tau_0\exp(E_a/RT)$, where τ_0 is the correlation time at the limit infinite temperature, E_a – the height of the barrier, and R – gas constant. After the fitting procedure, the activation energy E_a and the correlation time τ_c were estimated as $E_{a3} = 19.7$ kJ mol^{-1}, $\tau_c = 6.2 \times 10^{-14}$ s and relaxation constant $C = 1.5 \times 10^9$ s^{-2}, respectively. Theoretical curves corresponding to the above fitting are depicted as the red curves in Fig. 9. The E_{a3} energy is assigned to the reorientation of the cations about the C_3–N_1 axis. Worth noting is that similar T_1 *vs.* $1/T$ function behaviour was observed for (azetidinium)$_2$KCo(CN)$_6$[42] in comparable temperature regions.

The temperature dependence of the second moment (M_2) is presented in Fig. S9 (ESI†). According to these results the drastic reduction of M$_2$ at *ca.* 167 K is due to the fact that the ring-puckering movement of cations starts abruptly above the (**IV → III**) PT temperature. The contribution of the pyrrolidinium cations to the molecular mechanism of this transition is in accordance with the structural results.

2.8. Photoluminescence properties

The remarkable properties presented above encouraged us to study the luminescence of **AZECdCl₃**. Since the material revealed only weak blue luminescence upon UV excitation at room temperature, the optical properties of **AZECdCl₃** were examined for the solid-state powder specimen in the broad 15–300 K temperature range. Fig. 10 presents the photoluminescence emission (PL) spectra recorded at 281 nm (Fig. 10a) and 291 nm (Fig. 10b) excitation (for clarity, in the whole PL/PLE section, measurements for a given temperature are drawn in one color). Independently of the excitation wavelength, the spectra structure is analogous, and two emission areas are evident. Namely, in the range of 330–480 nm there is a narrower emission band and there is a broader one covering the 500–750 nm range. With the increase of temperature, the luminescence disappears so that above 250 K, PL is barely visible, as mentioned before, revealing a significant thermal quenching in **AZECdCl₃**. This process is well known for other cadmium halides crystals[43,44] and its hybrid compounds.[45,46]

The photoluminescence excitation spectra (PLE) of **AZECdCl₃** in Fig. S10 (ESI†) demonstrate structured bands with peaks at about 280 nm and 290 nm suggesting the origin of bands from different excited states. Furthermore, comparison of non-normalized PL spectra (Fig. 10) and those normalized to the same peak intensity (Fig. S11, ESI†) shows that there are no drastic differences between these two excitation wavelengths.
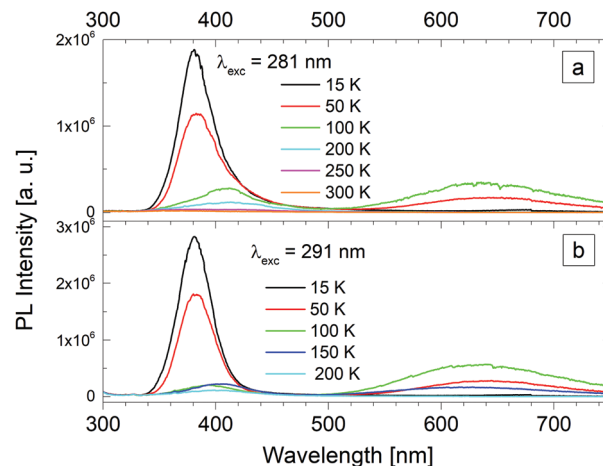

Fig. 10 Temperature dependence of photoluminescence emission (PL) spectra of **AZECdCl₃** excited with (a) 281 nm and (b) 291 nm.

Also, there is another common feature, namely in both cases the decrease in temperature from 200 K to 100 K increases the intensity of low-energy emission at 620 nm. Further cooling to 15 K in turn causes its disappearance with a simultaneous shift of high-energy band from 410 nm to 380 nm and increase of the total emission intensity accompanied by the band narrowing. In more detail, it is shown in Fig. S12 (ESI†). At 15 K, the emission is fitted well by a Gaussian distribution function with one component, as shown in Fig. S13 (ESI†), with a FWHM of 34 nm.

The measured PL decay times of the studied compound range from 2.1 ms to 28.7 ns (370 nm), 4.1 μs to 130 ns (410 nm) and 9.2 μs to 4.4 μs (620 nm) with heating (Table S7 and Fig. S14, ESI†). In the literature, a spread in PL lifetimes of hybrid halides is reportedly ranging from subnanoseconds up to 54.1 ns,[47–49] attributed to self-trapped excitonic states (STEs). Also, phosphorescence lifetimes in the microsecond range are reported.[50,51] It is worth noting that at 100 K both the low and high energy emission are excited through the same wavelength 281 and 291 nm and have similar lifetime of few μs, indicating fast thermal equilibrium between their excited states.

In hybrid metal halide perovskites, tunable broadband emission has been attributed to structural distortions,[47,52,53] particularly to the distortions of the inorganic MX₆ octahedra.[45,54] According to X-ray analysis, the [CdCl₆]$^{4-}$ octahedra distortion changes increased with lowering the temperature, particularly from 200 K to 100 K. For metal–halide systems, PL may originate from the presence of free and biexcitons,[55] free exciton and exciton–phonon interactions,[55] or free and bound excitons.[55] Taking into account the relatively long PL lifetime of **AZECdCl₃**, the origin of spin-forbidden triplet exciton emission is possible.[56] Furthermore, emission might also originate from structural phase transitions often observed in these hybrids[57,58] which may apply in **AZECdCl₃** as structural phase transitions occur in the examined temperature range. The presented studies suggest that the bluish emission in **AZECdCl₃** likely has contributions from both distorted

This journal is © The Royal Society of Chemistry 2022

J. Mater. Chem. C, 2022, **10**, 3036–3047 | 3043

excited states due to strong electron–phonon coupling in a deformable lattice as well as inhomogeneous broadening resulting from a distribution of trap states.

3. Conclusions

In this contribution we have introduced a novel azetidinium-based organic–inorganic hybrid perovskite of formula [C$_3$H$_8$N]CdCl$_3$ (**AZECdCl$_3$**), hosting ferroelectric, ferroelastic and SHG-off–SHG-on quadratic switching properties. Indeed, structural, dielectric and SHG measurements show that **AZECdCl$_3$** loses the inversion centre at a temperature of 202 K, and in the subsequent transition, it regains it again around a temperature of 167K (Scheme 1). Ferroelectric order is present only in phase **III** with a temperature window of ∼40 K. Polarization switching was proven by the pyroelectric effect and hysteresis loop measurements with $P_s \approx 4$ μC cm^{-2} (168 K). This high value of bulk polarization is corroborated by theoretical calculations. The relatively small coercive field and the low impact of the field frequency on the value of spontaneous polarization also sets out the title compound from other Cd(II) based ferroelectrics. Polarizing microscope observations show that ferroelastic properties span across three adjacent phases **II**, **III** and **IV**, whereas phase **I** appears to be the only paraelastic phase. The observed reversible transformation of the first type between the polar (**III**) and low temperature centrosymmetric phase (**IV**) allowed us also to demonstrate uncommon type of NLO switching, in which the lower temperature phase is SHG inactive, while the higher temperature phase is SHG active, yielding SHG-off–SHG-on solid-state switching

The dynamics of the polar cations located between 1-D inorganic chains are responsible for thermally induced three-stage PTs (Scheme 1). Analysis of the dielectric response close to T_c suggests that the mechanism of the paraelectric–ferroelectric transition is mixed; the "displacive" contribution is due to the strong distortion of both cationic and anionic substructures and the "order–disorder" contribution is assigned to very fast reorientational motion of dipolar cations. The latter contribution is very small, and the relaxation process related to the dynamics of cations will be shifted to the microwave range. The molecular dynamics of the azetidinium cations were also investigated using ^{1}HNMR measurements in the solid-state. These measurements confirm that the ring-puckering movement of cations starts abruptly above the (**IV** → **III**) PT temperature. These measurements confirm that the ring-puckering movement of cations starts abruptly above the
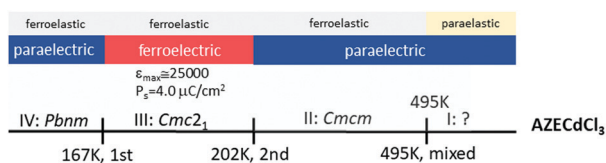
(**IV** → **III**) PT temperature. It appears that structural deformations of the crystal play a crucial role in the observed temperature-dependent photoluminescence and favour exciton self-trapping. Bluish triplet exciton emission is suggested by the relatively long photoluminescence lifetimes.

4. Experimental

4.1. Synthesis

3 g of CdCO$_3$ was suspended in deionized water, and then concentrated hydrochloric acid was added dropwise to the solution until completely dissolved. Next, azetidine (Sigma-Aldrich, 98%, 1 g) was added in part to the solution placed in an ice bath. If necessary, a few drops of the appropriate acid were added. By slow evaporation at room temperature, white-transparent crystals of **AZECdCl$_3$**:[C$_3$H$_8$N]CdCl$_3$ in the shape of the block were obtained (see Fig. 11). The composition of the compound was confirmed by elemental analysis to be C: 13.2% (theor. 13.01%), N: 5.01% (theor. 5.06), H 2.96% (theor. 2.91). A powder X-ray diffraction verified the phase purity (see Fig. S15, ESI†). XRD patterns were recorded in the range of $2\theta = 5$–80° with the step $2\theta = 0.024°$ and 1 s counting time using a D8 Advance X-ray Diffractometer from Bruker. The Ni-filtered Cu K$_{\alpha1}$ radiation ($\lambda = 1.540596$ Å) from a Cu X-ray tube was applied.

4.2. Thermal analysis.
DSC measurements were performed by heating and cooling of the polycrystalline sample in the temperature range of 160–480 K with a ramp rate of 10 K min^{-1} using a Metler Toledo DSC 3 instrument. The TGA/DSC measurements were performed on a TGA-DSC 3$^+$ instrument between 290 and 900 K with a ramp rate of 5 K min^{-1}. The scan was performed in flowing nitrogen (flow rate: 1 dm^3 h^{-1}).

4.3. Crystal structure determination

The single crystals of **AZECdCl$_3$** were mounted on a CCD Xcalibur, Sapphire2 diffractometer (graphite monochromatic, Mo Kα radiation, $\lambda = 0.71073$ Å). The measurements have been performed at 220.0(1), 185.0(1) and 100.0(1) K. The corrections to the Lorentz, polarisation factors and absorption were applied to the reflection intensities.[59] The structures were solved by direct methods applying the SHELX program package.[60] The hydrogen atoms were determined from the geometric concepts and refined in a riding model with isotropic temperature factors of 1.2 times the U_{eq} value of the parent atom. All

Scheme 1 The phase diagram of **AZECdCl$_3$**. 1st: first-order PT, 2nd: second-order PT.

Fig. 11 Single crystals of **AZECdCl$_3$** crystallized from aqueous solutions.

3044 | *J. Mater. Chem. C*, 2022, **10**, 3036–3047

This journal is © The Royal Society of Chemistry 2022

non-hydrogen atoms were located from the difference Fourier synthesis and refined by the least-squares method in the full-matrix anisotropic approximation. The crystallographic data for the compound and details of the X-ray experiment are collected in Table S1 (ESI†). Crystal structure figures were constructed using Mercury[61] software. CCDC 2107086–2107088.†

4.4. Electrical measurements

Electrical measurements were performed on the crystallographically oriented crystal. Single crystals were cut perpendicularly to the (a) a-axis (S = 4 mm^2, d = 1.1 mm), (b) b-axis (S = 16 mm^2, d = 0.82 mm), and (c) c-axis (S = 4 mm^2, d = 0.7 mm). The complex dielectric permittivity was measured between 150 and 300 K using an Agilent E4980A Precision LCR Meter in the frequency range of 135 Hz–2 MHz. The temperature was stabilized and controlled using an INSTEC STC200. The electric measurements were carried out in a controlled nitrogen atmosphere. The pyroelectric properties were tested with a Keithley 6517D electrometer/high resistance meter between 180 and 300 K, with a temperature ramp of 2 K min^{-1}. The ferroelectric hysteresis loop single crystals cut in directions perpendicular to the c-axis were obtained by using a Sawyer–Tower circuit Precision Premier II (Radiant Technologies, Inc.). The surfaces of the crystal were coated with silver conductive paint (Electron Microscopy Sciences, 503).

4.5. Temperature-resolved second-harmonic generation (TR-SHG) and Kurtz–Perry study

TR-SHG studies and the Kurtz–Perry test were performed using a Coherent Astrella Ti:sapphire regenerative amplifier. This laser delivers 800 nm pulses of ∼75 fs length and operates at a repetition rate of 1 kHz. The single crystals of **AZECdCl$_3$** and potassium dihydrogen phosphate (KDP, used as a reference for the Kurtz–Perry test) were crushed with a spatula and sieved through a mini-sieve set (Aldrich), obtaining a microcrystal size fraction of 125–177 µm. Next, size-graded samples were fixed between microscope glass slides (forming tightly packed layers), sealed, and mounted to the sample holder. The laser beam was directed onto a sample at 45° and was unfocused. Signal-collecting optics, mounted to the glass optical fiber, was placed perpendicularly to the plane of the sample (backscattering geometry). Scattered pumping radiation was suppressed with the use of a 700 nm short-pass dielectric filter (FESH0700, Thorlabs). All emission spectra were recorded using an Ocean Optics Flame T spectrograph.

The TR-SHG study (145–220 K with 2–3 K step) was conducted using an 800 nm unfocused beam, a mean power of 670 mW and an irradiation area of 0.7 cm^2. Temperature switching of SHG was performed by setting the temperature at 155 K and 167 K in an alternate manner, and at these temperature points the **AZECdCl$_3$** sample was irradiated using the same beam parameters as were used for the TR-SHG study. Temperature control of the sample was performed using a Linkam LTS420 heating/freezing stage.

4.6. Computational methods

Total-energy calculations were performed using a plane-wave basis set defined by the energy cut-off up to 500 eV coupled with Troullier–Martins type pseudopotentials[62] and dense Monkhorst–Pack k-point meshes.[63] Density functionals selected for the calculations are PBE (Perdew–Burke–Ernzerhof)[64] and LDA,[65] as implemented in the Abinit software suite.[66,67] The Berry phase method was used to calculate spontaneous polarisation.[37,38] A similar approach was successfully adopted to study the spontaneous polarisation in organic–inorganic hybrids (pyrrolidinium)$_3$[Sb$_2$Cl$_9$][68] and (pyrrolidinium)$_2$Cd$_2$I$_6$.[11] For further details see the ESI.†

4.7. ^{1}H NMR measurements

The spin–lattice relaxation time T_1 was measured using an ELLAB TEL-Atomic PS 15 spectrometer working at 25 MHz from 85 K to 380 K. The T_1 relaxation times were determined using a saturation recovery method. Errors of the measured T_1 values were estimated to be lower than 5%. The measurements of the proton NMR line second moment were carried out with a wide-line ELLAB TEL-Atomic CW Spectrometer operating at 26.8 MHz from 116 K to 340 K. The second moment values M$_2$ were calculated by numeral integration of the first derivative of an absorption line and corrected for the finite modulation amplitude. The temperature of the sample was automatically controlled using an UNIPAN 660 temperature unit with a Pt-100 sensor. The powdered sample of **AZECdCl$_3$** was degassed under a pressure of 10^{-5} Torr and sealed in glass ampoules.

4.8. Photoluminescence

Photoluminescence excitation (PLE) and emission (PL) spectra, as well as millisecond lifetime curves, were recorded with an FLS 980 Spectrofluorimeter from Edinburgh Instruments equipped with a 450 W Xe (continuous excitation) and 60 W pulse Xe lamp. The solid-state sample was mounted with silver glue on the copper holder of a closed-cycle helium cryostat from Lake Shore Cryotronics, Inc. All spectra were recorded in the 15–300 K temperature range with a 50 K step using a Hamamatsu R928P photomultiplier cooled to −20 °C and operating in the range of 200–850 nm. TMS302-X single grating excitation and emission monochromators of 30 cm focal lengths were used. The spectral resolution of all measurements was 0.3 nm. Nanosecond decay kinetic curves were obtained with the use of the EPLED-280 pulse laser (280 nm excitation) and an F-G05 low-noise Hamamatsu H5773-04 photomultiplier.

Author contributions

The manuscript was written through contributions from all authors. All authors have given approval to the final version of the manuscript. These authors contributed equally.

Conflicts of interest

There are no conflicts to declare.

This journal is © The Royal Society of Chemistry 2022

J. Mater. Chem. C, 2022, **10**, 3036–3047 | **3045**

Notes and references

1 W. Li, Z. Wang, F. Deschler, S. Gao, R. H. Friend and A. K. Cheetham, *Nat. Rev. Mater.*, 2017, **23**(2), 1–18.

2 L. W. Martin and A. M. Rappe, *Nat. Rev. Mater.*, 2016, **22**(2), 1–14.

3 A. Piecha-Bisiorek, A. Białońska, R. Jakubas, P. Zieliński, M. Wojciechowska and M. Gałązka, *Adv. Mater.*, 2015, **27**, 5023–5027.

4 Y. Zhang, Y. Liu, H. Y. Ye, D.-W. Fu, W. Gao, H. Ma, Z. Liu, Y. Liu, W. Zhang, J. Li, G.-L. Yuan and R. G. Xiong, *Angew. Chemie Int. Ed.*, 2014, **53**, 5064–5068.

5 W. Zhang and R. G. Xiong, *Chem. Rev.*, 2011, **112**, 1163–1195.

6 N. Leblanc, N. Mercier, L. Zorina, S. Simonov, P. Auban-Senzier and C. Pasquier, *J. Am. Chem. Soc.*, 2011, **133**, 14924–14927.

7 G. C. Xu, X. M. Ma, L. Zhang, Z. M. Wang and S. Gao, *J. Am. Chem. Soc.*, 2010, **132**, 9588–9590.

8 M. Šimėnas, A. Kultaeva, S. Balčiunas, M. Trzebiatowska, D. Klose, G. Jeschke, M. Mączka, J. Banys and A. Pöppl, *J. Phys. Chem. C*, 2017, **121**, 16533–16540.

9 Y. Zhang, H. Y. Ye, W. Zhang and R. G. Xiong, *Inorg. Chem. Front.*, 2014, **1**, 118–123.

10 Z. X. Wang, Y. Zhang, Y. Y. Tang, P. F. Li and R. G. Xiong, *J. Am. Chem. Soc.*, 2019, **141**, 4372–4378.

11 M. Rok, B. Zarychta, A. Bil, J. Trojan-Piegza, W. Medycki, A. Miniewicz, A. Piecha-Bisiorek, A. Ciżman and R. Jakubas, *J. Mater. Chem. C*, 2021, **9**, 7665–7676.

12 M. Rok, P. Starynowicz, A. Ciżman, J. K. Zaręba, A. Piecha-Bisiorek, G. Bator and R. Jakubas, *Inorg. Chem.*, 2020, **59**, 11986–11994.

13 P. F. Li, W. Q. Liao, Y. Y. Tang, H. Y. Ye, Y. Zhang and R. G. Xiong, *J. Am. Chem. Soc.*, 2017, **139**, 8752–8757.

14 L. Zhou, P. P. Shi, X. M. Liu, J. C. Feng, Q. Ye, Y. F. Yao, D. W. Fu, P. F. Li, Y. M. You, Y. Zhang and R. G. Xiong, *NPG Asia Mater.*, 2019, **11**, 15.

15 K. Gesi, *J. Phys. Soc. Jpn.*, 1990, **59**, 432–434.

16 H. Y. Ye, Y. Zhang, D. W. Fu and R. G. Xiong, *Angew. Chem., Int. Ed.*, 2014, **53**, 11242–11247.

17 W. J. Xu, C. T. He, C. M. Ji, S. L. Chen, R. K. Huang, R. B. Lin, W. Xue, J. H. Luo, W. X. Zhang and X. M. Chen, *Adv. Mater.*, 2016, **28**, 5886–5890.

18 Y. Y. Tang, Y. Ai, W. Q. Liao, P. F. Li, Z. X. Wang and R. G. Xiong, *Adv. Mater.*, 2019, **31**, 1–6.

19 S. Deswal, S. K. Singh, R. Pandey, P. Nasa, D. Kabra, B. Praveenkumar, S. Ogale and R. Boomishankar, *Chem. Mater.*, 2020, **32**, 8333–8341.

20 S. Deswal, S. K. Singh, P. Rambabu, P. Kulkarni, G. Vaitheeswaran, B. Praveenkumar, S. Ogale and R. Boomishankar, *Chem. Mater.*, 2019, **31**, 4545–4552.

21 V. Jella, S. Ippili, J. H. Eom, S. V. N. Pammi, J. S. Jung, V. D. Tran, V. H. Nguyen, A. Kirakosyan, S. Yun, D. Kim, M. R. Sihn, J. Choi, Y. J. Kim, H. J. Kim and S. G. Yoon, *Nano Energy*, 2019, **57**, 74–93.

22 Y. Hu, L. You, B. Xu, T. Li, S. A. Morris, Y. Li, Y. Zhang, X. Wang, P. S. Lee, H. J. Fan and J. Wang, *Nat. Mater.*, 2021, **20**, 612–617.

23 R. Guo, Y. Guo, H. Duan, H. Li and H. Liu, *ACS Appl. Mater. Interfaces*, 2017, **9**, 8271–8279.

24 H. Van Ngoc and D. Joon Kang, *Nanoscale*, 2016, **8**, 5059–5066.

25 S.-H. Shin, Y.-H. Kim, M. H. Lee, J.-Y. Jung and J. Nah, *ACS Nano*, 2014, **8**, 2766–2773.

26 K.-I. Park, J. Hwan Son, G.-T. Hwang, C. Kyu Jeong, J. Ryu, M. Koo, I. Choi, S. Hyun Lee, M. Byun, Z. Lin Wang, K. Jae Lee, K. Park, J. H. Son, G. Hwang, C. K. Jeong, M. Koo, I. Choi, S. H. Lee, M. Byun, K. J. Lee, J. Ryu and Z. L. Wang, *Adv. Mater.*, 2014, **26**, 2514–2520.

27 R. T. Williams and K. S. Song, *J. Phys. Chem. Solids*, 1990, **51**, 679–716.

28 D. Cortecchia, J. Yin, A. Petrozza and C. Soci, *J. Mater. Chem. C*, 2019, **7**, 4956–4969.

29 K. Robinson, G. V. Gibbs and P. H. Ribbe, *Science*, 1971, **172**, 567–570.

30 M. Rok, A. Ciżman, B. Zarychta, J. K. Zaręba, M. Trzebiatowska, M. Mączka, A. Stroppa, S. Yuan, A. E. Phillips and G. Bator, *J. Mater. Chem. C*, 2020, **8**, 17491–17501.

31 J.-X. Gao, X.-N. Hua, X.-G. Chen and W.-Q. Liao, *J. Mater. Chem. C*, 2019, **5348**, 5348.

32 X. Liu, C. Ji, Z. Wu, L. Li, S. Han, Y. Wang, Z. Sun and J. Luo, *Chem. – Eur. J.*, 2019, **25**, 2610–2615.

33 J. Zhang, S. Han, X. Liu, Z. Wu, C. Ji, Z. Sun and J. Luo, *Chem. Commun.*, 2018, **54**, 5614–5617.

34 Z. Wu, X. Liu, C. Ji, L. Li, S. Wang, Z. Sun, W. Zhang, Y. Peng and J. Luo, *J. Mater. Chem. C*, 2018, **6**, 9532–9536.

35 L. Xu, J. X. Gao, X. G. Chen, X. N. Hua and W. Q. Liao, *Dalton Trans.*, 2018, **47**, 16995–17003.

36 K. Yoshimitsu and T. Matsubara, *Prog. Theor. Phys. Suppl.*, 1968, **E68**, 109–136.

37 D. Vanderbilt and R. D. King-Smith, *Phys. Rev. B*, 1993, **48**, 4442–4455.

38 R. D. King-Smith and D. Vanderbilt, *Phys. Rev. B*, 1993, **47**, 1651–1654.

39 P. Szklarz, J. Zaleski, R. Jakubas, G. Bator, W. Medycki and K. Falińska, *J. Phys.: Condens. Matter*, 2005, **17**, 2509.

40 A. Piecha, R. Jakubas, A. Pietraszko, J. Baran, W. Medycki and D. Kruk, *J. Solid State Chem.*, 2009, **182**, 2949–2960.

41 N. Bloembergen, E. M. Purcell and R. V. Pound, *Phys. Rev.*, 1948, **73**, 679–712.

3046 | *J. Mater. Chem. C*, 2022, **10**, 3036–3047

This journal is © The Royal Society of Chemistry 2022

42 T. Asaji, *Bull. Chem. Soc. Jpn.*, 2021, **94**, 1659–1663.

43 S. Kawabata, M. Kitaura and H. Nakagawa, *Phys. Status Solidi C Conf.*, 2005, **2**, 53–56.

44 H. Matsumoto and H. Nakagawa, *J. Lumin.*, 1979, **18/19**, 19–22.

45 A. Yangui, S. Pillet, E. E. Bendeif, A. Lusson, S. Triki, Y. Abid and K. Boukheddaden, *ACS Photonics*, 2018, **5**, 1599–1611.

46 Z. Qi, Y. Chen, Y. Guo, X. Yang, F. Q. Zhang, G. Zhou and X. M. Zhang, *J. Mater. Chem. C*, 2021, **9**, 88–94.

47 L. Mao, Y. Wu, C. C. Stoumpos, B. Traore, C. Katan, J. Even, M. R. Wasielewski and M. G. Kanatzidis, *J. Am. Chem. Soc.*, 2017, **139**, 11956–11963.

48 G. E. Wang, G. Xu, M. S. Wang, L. Z. Cai, W. H. Li and G. C. Guo, *Chem. Sci.*, 2015, **6**, 7222–7226.

49 M. D. Smith and H. I. Karunadasa, *Acc. Chem. Res.*, 2018, **51**, 619–627.

50 C. Zhou, H. Lin, H. Shi, Y. Tian, C. Pak, M. Shatruk, Y. Zhou, P. Djurovich, M. H. Du and B. Ma, *Angew. Chem., Int. Ed.*, 2018, **57**, 1021–1024.

51 H. Nakagawa, K. Hayashi and H. Matsumoto, *J. Phys. Soc. Jpn.*, 1977, **43**, 1655–1663.

52 E. R. Dohner, A. Jaffe, L. R. Bradshaw and H. I. Karunadasa, *J. Am. Chem. Soc.*, 2014, **136**, 13154–13157.

53 L. Mao, Y. Wu, C. C. Stoumpos, M. R. Wasielewski and M. G. Kanatzidis, *J. Am. Chem. Soc.*, 2017, **139**, 5210–5215.

54 A. Yangui, D. Garrot, J. S. Lauret, A. Lusson, G. Bouchez, E. Deleporte, S. Pillet, E. E. Bendeif, M. Castro, S. Triki, Y. Abid and K. Boukheddaden, *J. Phys. Chem. C*, 2015, **119**, 23638–23647.

55 J. I. Fujisawa and T. Ishihara, *Phys. Rev. B: Condens. Matter Mater. Phys.*, 2004, **70**, 1–6.

56 S. Liu, X. Fang, B. Lu and D. Yan, *Nat. Commun.*, 2020, **11**, 1–9.

57 A. Yangui, S. Pillet, A. Mlayah, A. Lusson, G. Bouchez, S. Triki, Y. Abid and K. Boukheddaden, *J. Chem. Phys.*, 2015, **143**, 224201.

58 A. Yangui, S. Pillet, D. Garrot, S. Triki, Y. Abid and K. Boukheddaden, *J. Appl. Phys.*, 2015, **117**, 115503.

59 CrysAlis RED, CrysAlis CCD, Oxford Diffraction, Oxford Diffraction Ltd, Abingdon, England, 2008.

60 G. M. Sheldrick, *Acta Crystallogr., Sect. C: Struct., Chem.*, 2015, **71**, 3–8.

61 C. F. MacRae, I. Sovago, S. J. Cottrell, P. T. A. Galek, P. McCabe, E. Pidcock, M. Platings, G. P. Shields, J. S. Stevens, M. Towler and P. A. Wood, *J. Appl. Crystallogr.*, 2020, **53**, 226–235.

62 N. Troullier and J. L. Martins, *Phys. Rev. B*, 1991, **43**, 8861–8869.

63 H. J. Monkhorst and J. D. Pack, *Phys. Rev. B*, 1976, **13**, 5188–5192.

64 J. Perdew, K. Burke and M. Ernzerhof, *Phys. Rev. Lett.*, 1996, **77**, 3865–3868.

65 D. M. Ceperley and B. J. Alder, *Phys. Rev. Lett.*, 1980, **45**, 566–569.

66 X. Gonze, J. M. Beuken, R. Caracas, F. Detraux, M. Fuchs, G. M. Rignanese, L. Sindic, M. Verstraete, G. Zerah, F. Jollet, M. Torrent, A. Roy, M. Mikami, P. Ghosez, J. Y. Raty and D. C. Allan, *Comput. Mater. Sci.*, 2002, **25**, 478–492.

67 X. Gonze, F. Jollet, F. Abreu Araujo, D. Adams, B. Amadon, T. Applencourt, C. Audouze, J. M. Beuken, J. Bieder, A. Bokhanchuk, E. Bousquet, F. Bruneval, D. Caliste, M. Cote, F. Dahm, F. Da Pieve, M. Delaveau, M. Di Gennaro, B. Dorado, C. Espejo, G. Geneste, L. Genovese, A. Gerossier, M. Giantomassi, Y. Gillet, D. R. Hamann, L. He, G. Jomard, J. Laflamme Janssen, S. Le Roux, A. Levitt, A. Lherbier, F. Liu, I. Lukačević, A. Martin, C. Martins, M. J. T. Oliveira, S. Ponce, Y. Pouillon, T. Rangel, G. M. Rignanese, A. H. Romero, B. Rousseau, O. Rubel, A. A. Shukri, M. Stankovski, M. Torrent, M. J. Van Setten, B. Van Troeye, M. J. Verstraete, D. Waroquiers, J. Wiktor, B. Xu, A. Zhou and J. W. Zwanziger, *Comput. Phys. Commun.*, 2016, **205**, 106–131.

68 M. Wojciechowska, A. Gagor, A. Piecha-Bisiorek, R. Jakubas, A. Cizman, J. K. Zaręba, M. Nyk, P. Zieliński, W. Medycki and A. Bil, *Chem. Mater.*, 2018, **30**, 4597–4608.

This journal is © The Royal Society of Chemistry 2022

J. Mater. Chem. C, 2022, **10**, 3036–3047 | 3047